This manuscript has been authored by UT-Battelle, LLC under Contract No. DE-AC05-00OR22725 with the U.S. Department of Energy. The United States Government retains and the publisher, by accepting the article for publication, acknowledges that the United States Government retains a non-exclusive, paid-up, irrevocable, world-wide license to publish or reproduce the published form of this manuscript, or allow others to do so, for United States Government purposes. The Department of Energy will provide public access to these results of federally sponsored research in accordance with the DOE Public Access Plan (http://energy.gov/downloads/doe-public-access-plan).

Defect genome of cubic perovskites for fuel cell applications

Janakiraman Balachandran[1*], Lianshan Lin[2], Jonathan S. Anchell[1], Craig A. Bridges[3], P. Ganesh[1*]

[1]Center for Nanophase Materials Sciences, Oak Ridge National Laboratory, Oak Ridge, TN 37831

[2]Material Science and Technology Division, Oak Ridge National Laboratory, Oak Ridge, TN 37831

[3]Chemical Sciences Division, Oak Ridge National Laboratory, Oak Ridge, TN 37831

KEYWORDS. High-throughput, materials genome, defect genome, perovskites, point defects, fuel cells, proton conductors, oxides,

ABSTRACT: Heterogeneities such as point defects, inherent to material systems, can profoundly influence material functionalities critical for numerous energy applications. This influence in principle can be identified and quantified through development of large defect datasets which we call the defect genome, employing high-throughput *ab initio* calculations. However, high-throughput screening of material models with point defects dramatically increases the computational complexity and chemical search space, creating major impediments towards developing a defect genome. In this work, we overcome these impediments by employing computationally tractable *ab initio* models driven by highly scalable workflows, to study formation and interaction of various point defects (e.g. O vacancies, H interstitials and Y substitutional dopant), in over eighty cubic perovskites, for potential proton conducting ceramic fuel cell (PCFC) applications. The resulting defect datasets identify several promising perovskite compounds that can exhibit high proton conductivity. Further, the datasets also enable us to identify and explain, insightful and novel correlations between defect energies, material identities and defect induced local structural distortions. Such defect datasets and resultant correlations are necessary to build statistical machine learning models, which are required to accelerate discovery of new materials.

INTRODUCTION

The exponential increase in parallel computing and data storage capabilities over the last decade has revolutionized the way we conduct computational material science. By adopting a 'high-throughput' or 'materials genome' approach[1,2], it has become possible to computationally screen numerous candidate materials for the desired functionality. Publicly sharing such computed materials data, as done by several projects such as the Materials Project[3], AFLOW[4], CHiMAD[5], OQMD[6] and NOMAD[7], has further accelerated discovery of new materials pertaining to CO_2 capture[8], piezoelectrics[9], bulk metallic glasses[10], photovoltaics[11] and many more applications. To date, the materials screened by such high-throughput approach have been mainly restricted to ideal defect free compounds. However, real materials inherently possess various forms of heterogeneities – ranging from point defects to extended defects, such as dislocations, disclinations, grain-boundaries, precipitates and interfaces. In particular, point defects such as intrinsic vacancies, substitutional dopants and interstitials (both intrinsic and extrinsic) are known to profoundly influence the functional properties of materials[12–14]. Therefore, the next natural extension of the materials genome is the creation of large defect datasets (*aka* defect genome) by systematically screening such functional heterogeneities across numerous candidate materials.

These large defect datasets would contain information regarding the defect formation, interaction and migration energies across numerous material compounds and their influence on material properties. This information would be useful in identifying structure-composition-property trends. These insightful trends can enable us to build cheap statistical machine learning models that can accelerate the search for new materials[15–17]. Such large point defect datasets in solids can in principle be created using well established *ab initio* based computations[14]. However, the major challenges in developing them are due to the dramatic increase in (i) the computational complexity of the material models[14,18,19] and (ii) the vast combinatorial chemical search space upon introducing point defects in solid compounds.

The increase in computational complexity can be addressed by creating systematic model approximations. One such example is a recent modeling study by Emery *et.al*[20] to calculate oxygen vacancy formation energy in perovskites for thermochemical water splitting. They employ several approximations in their models, such as small size super-cells (of size 2x1x1) and ignoring structural relaxations, to keep the calculations tractable. However, such approximations are application dependent. For example, proton conducting ceramic fuel cells (PCFC) materials exhibit large anionic sub-lattice distortions upon proton uptake.[21,22] Hence, ignoring structural relaxations is not a valid approximation. In addition, we are also interested in studying defect complex which typically require much larger supercells.

Screening across vast chemical search space can be achieved through automated workflows that can create inputs, submit calculations, handle errors and parse output to store them in databases.[23] However, to perform such screening in a short span of time, the workflow needs to efficiently scale and take advantage of the existing massively parallel supercomputing architectures. In this work, we develop and employ such a workflow to systematically screen defects in one of the several possible

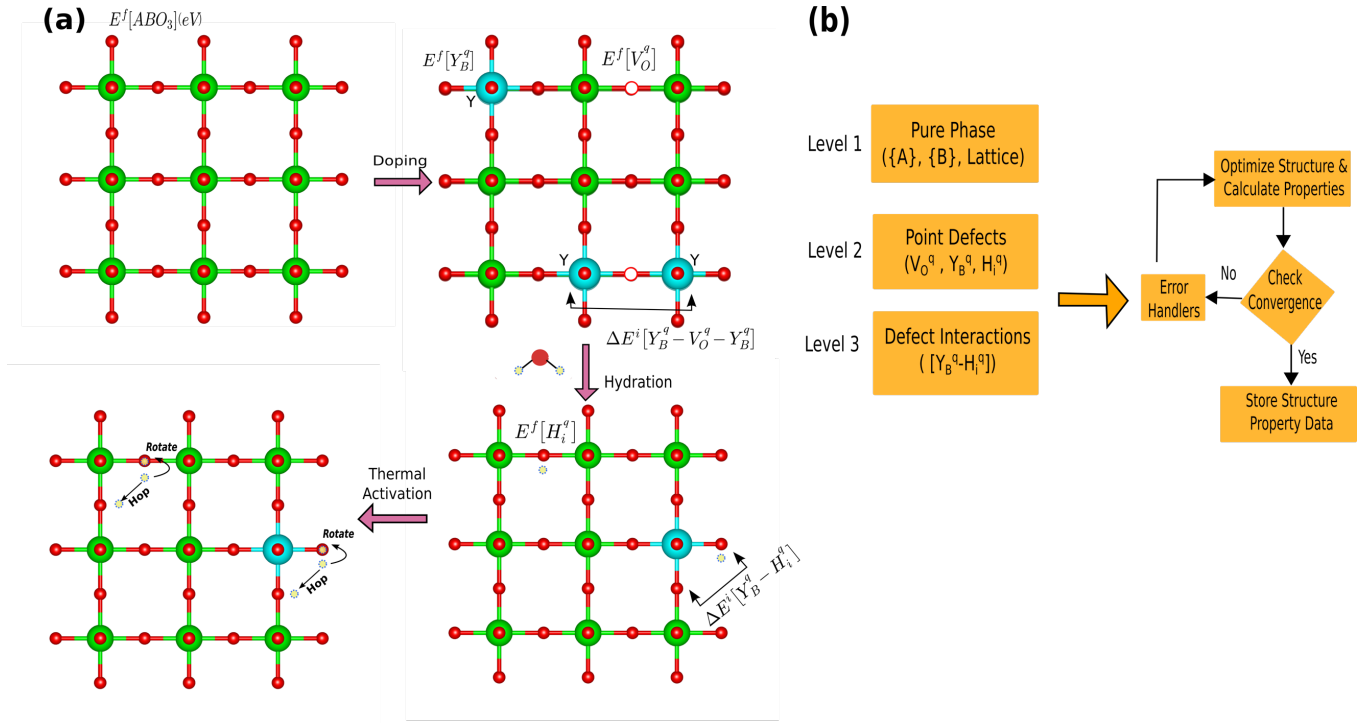

Figure.1. (a) Proton transport mechanism and relevant energetics in a prototypical perovskite material such as Y doped BaZrO3. (b)Flowchart of the high-throughput computational framework employed in this study to systematically predict defect energetics.

material/energy-application combinations – namely cubic perovskites for potential application in proton conducting ceramic fuel cells (PCFC).

Proton conducting Ceramic Fuel Cells (PCFC)

Solid-oxide fuel cells (SOFCs) are electrochemical energy conversion systems that can process wide range of fuels, such as H_2, CH_4 etc.[24,25] SOFCs operate at high temperatures (>800°C) by selectively transporting oxygen ions[26,27] across solid ceramic based electrolytes such as yttria stabilized zirconia, (YSZ). Proton conducting ceramic fuel cells (PCFC) on the other hand can operate at relatively lower temperatures (~400-600°C) by selectively transporting protons, since the small, singly-charged protons require lower activation energy for transport than the large doubly-charged oxygen ions.[28–30] This lowering of operating temperature can greatly improve material reliability and operational efficiency.

Proton transport across the PCFC materials underpins the overall performance of the technology. The mechanism of proton transport in solid oxide materials is shown in Fig.1(a). Protons cannot be spontaneously introduced via hydration in pure perovskites such as $BaZrO_3$. Substitutional doping of the B-site (Zr in this case) with acceptor dopants, such as yttrium, creates charge compensating oxygen vacancy defects. These vacant sites can now be filled via hydration, introducing mobile protons into the material. Protons introduced in Y doped $BaZrO_3$ are known to interact with the dopant atoms,[31] that can influence their motion. Under PCFC operating conditions (400-600°C), protons exhibit short-range motion via the Grotthuss mechanism,[32,33] which in turn leads to long-range proton conduction.

Thus, the entire proton transport process involves a series of steps involving formation, interaction and migration of various types of point defects. The energies involved at each step of transport needs to be optimized to discover fast proton conducting material. Some of the fastest proton conducting PCFC materials discovered to-date are perovskites based compounds (electrolyte – $BaZr_{0.8}Y_{0.2}O_{3-\delta}$ (Y-BZO)[34], cathode – $BaCo_{0.4}Fe_{0.4}Zr_{0.1}Y_{0.1}O_{3-\delta}$(BCFZYo.1)[35]). These discoveries have been mostly driven by expensive and time-consuming experimental approaches. Hence, there is a clear opportunity for computational modeling approaches to contribute towards discovering new proton conducting materials.

One computational approach to accelerate the discovery is to create a genome of point defects by systematically screening for such defects across a wide range of perovskites. In this paper, we demonstrate this approach by creating a computational framework that performs *ab initio* calculations driven by highly scalable workflow to compute structure formation, defect formation and defect interaction energies in more than eighty different (2,4) ABO_3 cubic perovskites (where $A \in \{Mg, Zn, Cd, Ca, Hg, Sr, Ba\}$ and $B \in \{Mn, Si, Ge, V, Rh, Ti, Ru, Ir, Os, Sn, Hf, Zr\}$). These energies are correlated with different atomic, structural and chemical properties to identify and explain insightful trends. Further, the data obtained from this framework also identifies several promising candidates amongst this dataset. This general

framework can be readily applied to screen other new materials with defects for any given energy application.

THEORY AND COMPUTATIONAL DETAILS

The various structural and defect energies calculated in this work are described below. The structure formation energy ($E^f[ABO_3]$) required to form a (2,4) cubic perovskite structure is given by

$$E^f[ABO_3] = \frac{1}{n}(E^{tot}[n(ABO_3)]) - E^{tot}[AO] - E^{tot}[BO_2] \quad (1)$$

where $E^{tot}[n(ABO_3)]$ is the ground state energy of cubic perovskite supercell of size n. $E^{tot}[AO]$ and $E^{tot}[BO_2]$ are the ground state energies of the corresponding binary oxides. The binary oxide crystal structures required to calculate the energies were obtained from the Materials Project[3] database. A negative structure formation energy indicates that it is energetically favorable to form a cubic perovskite structure w.r.t to the binary oxides, while a positive value indicates that it is energetically unfavorable to form the structure.

The energy required to introduce an isolated substitutional dopant in the B site of perovskites with charge q is given by

$$E^f[Y_B^q] = E^{tot}[n(AY_{\frac{1}{n}}B_{1-\frac{1}{n}}O_3); q] + \mu_B + q\mu_e - E^{tot}[n(ABO_3)] - \mu_Y \quad (2)$$

$E^{tot}[n(AY_{\frac{1}{n}}B_{1-\frac{1}{n}}O_3); q]$ is the ground state energy of the supercell with a substitutional dopant at charge state q. Since yttrium is the most widely used dopant, we restrict this study to only Y atom as a substitutional dopant. We also restrict the charge state q to zero for all defect calculations, since we are interested in relative energies and trends across different materials. μ_e is the electrochemical potential of the electrons, that is conventionally approximated to be the valence band maximum. μ_B and μ_Y are the chemical potentials of B site and Y dopant atoms, that are obtained from the corresponding binary oxides as,

$$\mu_B = (E^{tot}[BO_2] - 2\mu_O)$$
$$\mu_Y = (E^{tot}[Y_2O_3] - 3\mu_O)$$

where μ_O is the chemical potential of oxygen and is defined based on recent literature[36] as

$$\mu_O = \frac{1}{2}(2E^{tot}[(O)] + \varepsilon_{O_2}^{coh})$$

Where $2E^{tot}[(O)]$ is the energy of an oxygen atom. From experimental data[37] we obtain the cohesive energy of oxygen molecule $\varepsilon_{O_2}^{coh}$ to be -5.21eV. The energy required to create an isolated oxygen vacancy defect ($E^f[V_O^q]$) with charge q is given by

$$E^f[V_O^q] = E^{tot}[n(ABO_{3-\frac{1}{n}}); q] + \mu_O + q\mu_e - E^{tot}[n(ABO_3)] \quad (3)$$

$E^{tot}[n(ABO_{3-\frac{1}{n}}); q]$ is the ground state energy of the supercell with an oxygen vacancy in charge state q.

The energy required to introduce an isolated H interstitial defect ($E^f[H_i^q]$) with charge q is given by

$$E^f[H_i^q] = E^{tot}[n(ABO_3H_{\frac{1}{n}}); q] + q\mu_e - E^{tot}[n(ABO_3)] - \mu_H \quad (4)$$

$E^{tot}[n(ABO_3H_{\frac{1}{n}}); q]$ is the ground state energy of the supercell with a H interstitial in charge state q. μ_H is the chemical potential of the H interstitial which is defined as

$$\mu_H = \frac{1}{2}(2E^{tot}[(H)] + 2E^{tot}[(O)] - \varepsilon_{H_2O}^{coh} - \mu_O)$$

From experimental reference data[37], we obtain the cohesive energy of water molecule $\varepsilon_{H_2O}^{coh}$ to be -10.07eV. The defect formation energies as defined here ($E^f[Y_B^q]$, $E^f[V_O^q]$, $E^f[H_i^q]$) needs to have a positive value to ensure that the material is stable against spontaneous formation of such defects.

Recent work[22,31] in Y doped $BaZrO_3$ has shown that H interstitials are attracted to dopant atoms and can get trapped near the dopant atoms. Hence, even in the dilute limit, it is important to understand the interactions between dopants and H interstitials, which can be electrostatically bound. The dopant-H interaction energy ($\Delta E^i[Y_B^q - H_i^q]$) is defined as the difference in the formation energy of the dopant-H defect complex ($E^f[Y_B^q - H_i^q]$) encompassing two interacting defects and the formation energy of the isolated defects. i.e.,

$$\Delta E^i[Y_B^q - H_i^q] = E^f[Y_B^q - H_i^q] - (E^f[Y_B^q] + E^f[H_i^q]) \quad (5)$$

A negative value indicates an attractive interaction between the dopant and H interstitial. Similarly, we also calculate the dopant-vacancy interaction energy ($\Delta E^i[Y_B^q - V_O^q - Y_B^q]$) as

$$\Delta E^i[Y_B^q - V_O^q - Y_B^q] = E^f[Y_B^q - V_O^q - Y_B^q] - (2E^f[Y_B^q] + E^f[V_O^q]) \quad (6)$$

we choose the model system to comprise of an oxygen vacancy trapped between 2 Y dopants (see Fig 1(a) in main manuscript for schematics), since this configuration exhibits the strongest interaction in Y doped BaZrO3[38,39]

The major source of errors in defect energies arise due to electrostatic interactions, elastic strain interactions and quantum-mechanical interactions. Since, the models here are performed for systems with neutral charge (q=0), the supercell finite size error corrections due to electrostatic interactions[14,40–42] can be safely ignored. The elastic strain interactions typically decay as $1/L^3$ [14,43]. Since, the models employed in this work correspond to large supercells (3x3x3), these elastic distortions are effectively captured. Finally, the effect of quantum-mechanical electronic interactions is quantified by performing hybrid functional based calculations for a few targeted systems as described in detail in the following sections.

The *ab initio* calculations to compute these energies were performed using density-functional theory based methods as implemented in VASP.[44,45] We employ the PBE exchange-correlation functional[46] and PAW based atomic pseudo potentials,[47] which have been previously used to successfully study proton transport properties of Y doped $BaZrO_3$.[21,38,48] We use a 3x3x3 supercell of the cubic perovskite structure containing about 135 atoms. A Monkhorst-Pack **k**-point mesh of 2x2x2 was used in all our supercell calculations. In case of defect free structures, the volume was relaxed keeping the cubic shape of the crystal intact. In case of defect calculations, only the internal atomic coordinates are relaxed while fixing the volume and shape of the crystal structure. The charge state of defects (q) is restricted to zero. The calculations are converged until the difference in total energy between two consecutive relaxation steps is less than 0.7E-03eV.

The *ab initio* model used in this work does not incorporate corrections for errors arising from electron correlations, charged defect interactions and entropic contributions.[14,18] However, the data obtained from these models are helpful in performing comparative analysis and identifying insightful trends. For example, the data correctly identifies that Y doped $BaZrO_3$ has high stability, small positive defect formation energy and small negative dopant-H interaction energy --- attributes that are needed for good proton conductivity.

The models are further numerically validated by comparing the defect energies obtained for Y doped $BaZrO_3$ against previously published results as shown in Table. S3 of the supplementary information (SI).

The computational complexity and the number of calculations (search space) increases as we traverse from pure phase compounds to isolated defects to defect-complexes. Maximizing the number of *ab initio* calculations that can be simultaneously performed is necessary to achieve scalability. To execute this, we divide our computations into multiple levels as shown in Fig.1(b). Level 1 comprises of calculations of pure phase structures to predict the structure formation energy ($E^f[ABO_3]$). Level 2 comprises of calculations containing an isolated point defect to predict defect formation energies such as (a) Oxygen vacancy formation energy ($E^f[V_O^0]$), (b) Yttrium dopant substitution energy ($E^f[Y_B^0]$) and (c) H interstitial formation energy ($E^f[H_i^0]$). Level 3 is employed to model defect complexes to predict defect interaction energies such as the dopant-H interaction energy ($\Delta E^i[Y_B^0 - H_i^0]$) reported in this work for yttrium dopants. Since, no two calculations in the same level are dependent on one another, they are simultaneously executed, thereby achieving maximal parallelization.

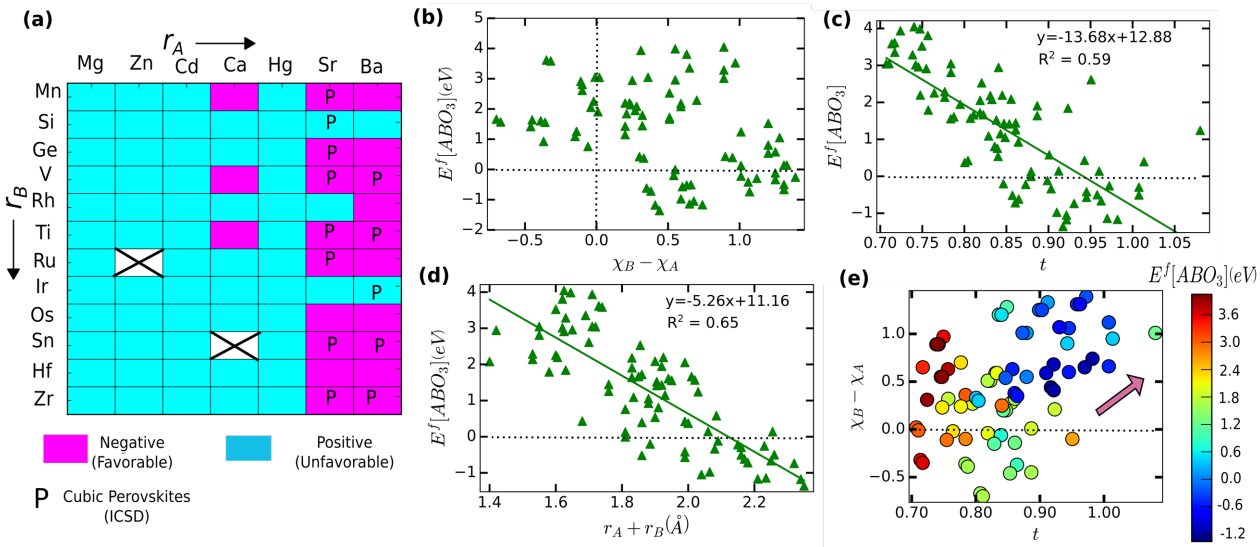

Figure.2 (a) Binary map of perovskite structure formation energy (favorable $E^f[ABO_3] < 0$ magenta and unfavorable ($E^f[ABO_3] > 0$ blue) for the various perovskites studied in this work. Reliable defect energies were not obtained for $ZnRuO_3$ and $CaSnO_3$ (marked in large cross), and hence are neglected from all subsequent analysis. (b-e) Scatter plot of perovskite structure formation energy ($E^f[ABO_3]$) as a function of various material identities such as (b) cationic electronegativity difference $\chi_B - \chi_A$ (c) tolerance factor t (d) sum of cationic radius $r_A + r_B$. The straight line indicates the linear regression fit without excluding any outliers. (e) Cross comparing($E^f[ABO_3]$) with $\chi_B - \chi_A$ and t identifies that most stable perovskites simultaneously possess high t and $\chi_B - \chi_A$ values.

The workflow that drives these multi-level *ab initio* calculations is created by integrating various open-source python codes derived from the Materials Project such as Pymatgen[49] (to create input data and parse output data), Fireworks[23] (workflow to launch simulations and store the IO data into MongoDB) and Custodian[49] (job management and error handler framework) along with an MPI bundler package developed by Oak ridge Leadership Computing Facility (OLCF) called *wraprun*[50]. The *wraprun* is a utility that wraps around multiple program multiple data (MPMD) mode of the aprun command in Cray environment in Titan supercomputer. The *wraprun* enables independent execution of multiple mpi applications under a single mpi call. This provides very efficient scaling (see Fig.S1 in SI) to potentially use the full

capacity of Titan through bundling of hundreds of *ab initio* calculations that were previously not feasible.

We also calculate the electronic structure of a few perovskites employing the hybrid exchange-correlation functional of Heyd, Scuseria, and Ernzerhof[51,52] at gamma k-point with 20% mixing for PBE atomic coordinates. This enables us to understand the influence of electronic interactions on comparative analysis of defect energies across perovskites.

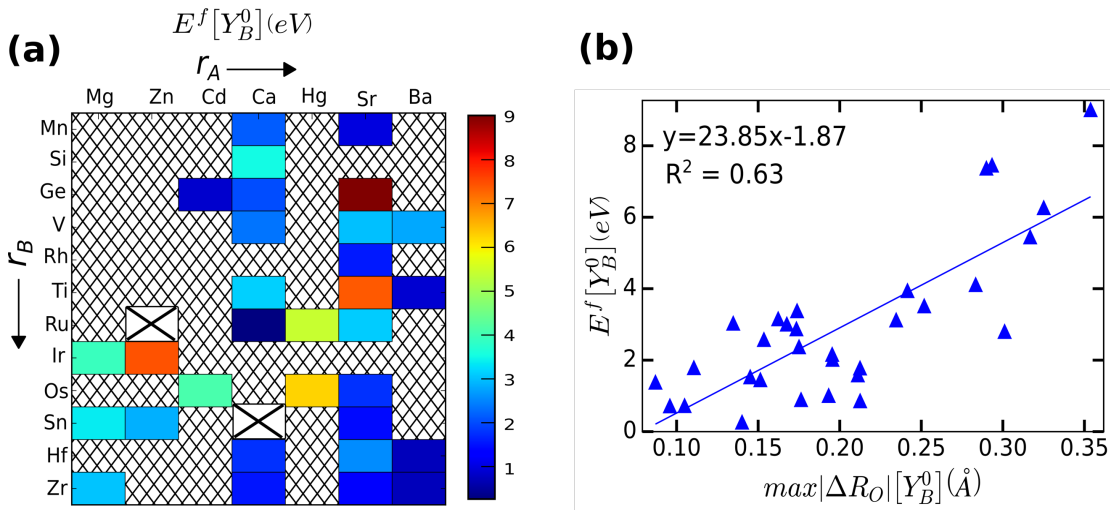

Figure.3. (a) Heatmap of small endothermic ([0,11] eV) Dopant substitution energy ($E^f[Y_B^0]$) – replacing existing B-site atom with Y dopant atom. Reliable defect energies were not obtained for $ZnRuO_3$ and $CaSnO_3$ (marked in large cross), and hence are neglected from all subsequent analysis. (b) Scatter plot and linear regression fit of dopant substitution energy ($E^f[Y_B^0]$) which increases (becomes more unfavorable to form) with increasing local distortion (quantified by the maximum oxygen displacement ($max|\Delta R_O|[Y_B^0]$)).

RESULTS AND DISCUSSION

Structure Formation Energy

We employ heatmaps and scatter plots (including linear regression fit where applicable) in this work to visualize and gain insights from the large volume of generated datasets. Fig. 2(a) shows a binary heatmap of all compositions with favorable ($E^f[ABO_3] < 0, magenta$) and unfavorable ($E^f[ABO_3] > 0, blue$) structure formation energy. The corresponding numerical heatmap of $E^f[ABO_3]$ is provided in Fig.S2 of the SI. As we could not obtain reliable defect energies for $ZnRuO_3$ and $CaSnO_3$, we exclude these two systems from all subsequent analysis. Fig.2(a) shows that perovskite formation is favored when the A site is occupied by a large alkaline earth metal atom, such as Ba, Sr and to some extent Ca. The symbol **P** denotes experimentally synthesized compounds found in the Inorganic Crystal Structure Database (ICSD) in cubic perovskite phase (*Pm-3m*). The computed $E^f[ABO_3]$ correctly identifies the favorability of perovskite formation in all these compounds except a few high-pressure phases such as $SrSiO_3$ and $BaIrO_3$ since our *ab initio* calculations were not performed at high pressures. Conversely, our calculations, also identify favorable cubic perovskite formation for compounds, not listed in ICSD in cubic perovskite polymorphs such as: $BaMnO_3$, $BaGeO_3$, $BaRhO_3$, $BaRuO_3$, $BaOsO_3$, $BaHfO_3$, $SrOsO_3$, $SrHfO_3$, $CaMnO_3$, $CaVO_3$ and $CaTiO_3$. Some of these compounds such as $CaTiO_3$ are known to crystalize in non-cubic perovskite phases (*Pbnm*[53]). Hence, we can reasonably expect to synthesize cubic perovskite polymorphs of these compounds through doping,[54,55] high-pressure synthesis[56] or via epitaxial strain[57].

To gain insights on how atomic, chemical and structural properties of the materials (*aka* material identities) influence $E^f[ABO_3]$, we correlate $E^f[ABO_3]$ with various combinations of electronegativity (cationic electronegativity difference ($\chi_B - \chi_A$)) and Shannon ionic radius (the Goldschmidt tolerance factor *(t)* and sum of cationic radius ($r_A + r_B$)). Fig.2(b) identifies that most stable perovskites have a large cationic electronegativity difference ($\chi_B - \chi_A \geq 0.35$). This is consistent with the proposition made by Kreuer[28] based on data from Sr and Ba based perovskites. However, for the wider range of perovskites studied it this work, a large electronegativity difference appears to be a necessary but not sufficient condition to describe favorable perovskite formation. This suggests that there are additional parameters that determine the stability of the cubic perovskite phase. Stability of perovskite structures is also typically thought to correlate with the Goldschmidt's tolerance factor *t*, defined as:

$$t = \frac{r_A + r_O}{\sqrt{2}(r_B + r_O)}$$

Upon performing linear regression as shown in Fig.2(c), ($E^f[ABO_3]$) exhibits inverse correlation (R^2=0.59) against *t*, wherein it becomes favorable to form cubic perovskites with increasing *t*. In fact, all stable cubic perovskites studied in this work possess high *t* value (t>0.85). This data is consistent with the previous empirical observations on experimentally synthesized perovskites[58–60] where most cubic perovskites typically exist for a *t* value between 0.9

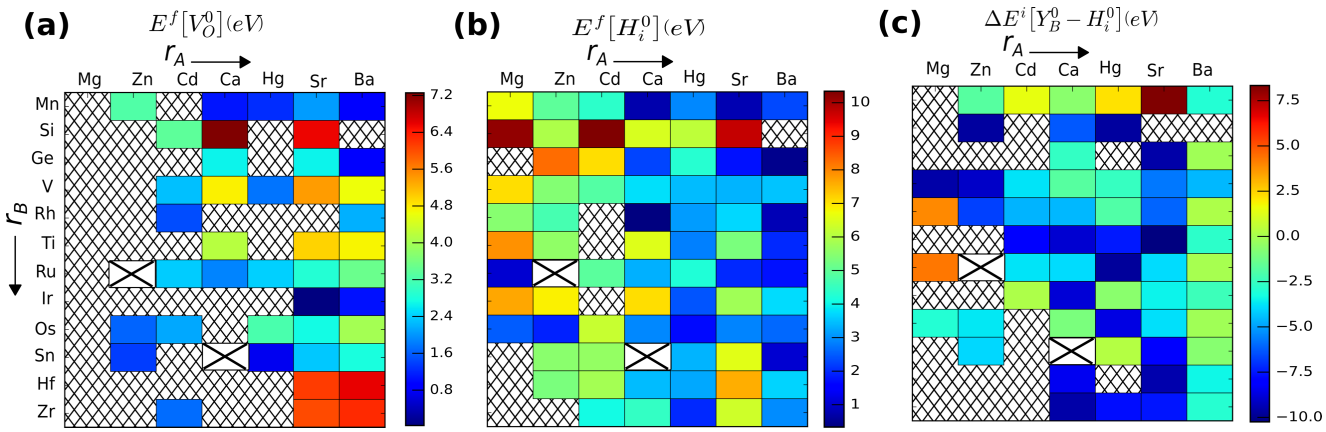

Figure.4. Heatmap of (a) Oxygen vacancy formation energy ($E^f[V_O^0]$) in range [0, 11] eV, (b) H interstitial formation energy $\left(E^f\left[H_i^0\right]\right)$ in range [0,11] eV, (c) Dopant-H interaction energy $\left(\Delta E^i\left[Y_B^0 - H_i^0\right]\right)$ in range [-11,9] eV.

and 1. Fig.2(d) displays a similar inverse correlation (R^2=0.65) between $E^f[ABO_3]$ and the sum of cationic radius $(r_A + r_B)$, suggesting that compounds with the largest A and B site atoms are more likely to form stable perovskite structures. Cross correlating material identities with $E^f[ABO_3]$ as shown in Fig. 1(e) identify that most stable cubic perovskite compounds simultaneously possess large $\chi_B - \chi_A$ and t values. Thus, any descriptor employed to predict the favorability of perovskite formation should typically be a function of $\chi_B - \chi_A$, t and $r_A + r_B$.

Defect Formation and Interaction Energies

We then proceed to calculate the defect formation and defect interaction energies for all the above described perovskite structures. This is motivated by our desire to identify material identities that exhibit universal correlation with defect energies. The defect formation energies need to be endothermic (>0eV) to ensure that the material is stable against spontaneous defect formation. Fig.3 provides a heat map of endothermic defect formation energies (in range [0,11] eV) and dopant-H interaction energy (in range [-11,9] eV). More details on excluded compounds are provided in Sec 2.1 of the SI.

From the heatmap of dopant substitution energy ($E^f[Y_B^0]$) as shown in Fig.3(a), we can observe that many compounds with large A-site atom show small, yet positive dopant substitution energies. Unfortunately, $E^f[Y_B^0]$ does not exhibit any quantitative linear correlation with these material identities.

Formation and interaction of point defects in material compounds can induce local distortions around them due to varied reasons such as size mismatch (e.g. local strain effect), or electrostriction (e.g. screening of local charges) or additional bonding (e.g. due to hydrogen-bond formation). Correlating defect energies with such local distortions can enable us to better understand the mechanisms that influence the formation and interaction of point defects. We quantify the local structural distortions by the maximum displacement of the O atom in the crystal structure upon introducing point defects. Fig.3(b) shows that $E^f[Y_B^0]$ exhibits linear positive correlation (R^2=0.63) with dopant induced local distortions ($max|\Delta R_O|[Y_B^0]$), wherein it becomes more unfavorable to dope the system with increasing distortion. A simple quantitative measure of local strain is the ionic radius difference between the dopant and the B-site atom $(r_D - r_B)$. The existence of correlation between $r_D - r_B$ and $max|\Delta R_O|[Y_B^0]$, demonstrated by a Pearson correlation coefficient value of 0.44 (where 1.0 indicating perfect positive correlation, -1.0 indicates perfect inverse correlation and 0.0 indicates no correlation), suggests that the higher the local strain, the more difficult it is to form substitutional dopants in these compounds.

Fig. 4(a) shows the heatmap for oxygen vacancy formation energy ($E^f[V_O^0]$). The $E^f[V_O^0]$ does not exhibit any quantitative correlations with material identities or oxygen vacancy induced local structural distortions.

Fig.4(b) shows heatmap of H interstitial formation energy ($E^f[H_i^0]$). Most compounds possess a positive $E^f[H_i^0]$. In particular, compounds with large A site cations such as Sr and Ba (and large t values) possess small positive $E^f[H_i^0]$. However, $E^f[H_i^0]$ does not exhibit good quantitative linear correlation with other material identities or the H interstitial induced local structural distortions.

Systems with dopant-H interaction energy ($\Delta E^i[Y_B^0 - H_i^0]$) between -11eV and 9eV is shown in Fig.3(d). We did not observe any quantitative correlations between $\Delta E^i[Y_B^0 - H_i^0]$ and the material identities or the local distortions.

Correlations in Favorable Compounds

The presence of relatively few quantifiable correlations among defect energies, material identities and local distortions indicate that unstable compounds could be suppressing the other intrinsic correlations. To unravel such suppressed correlations, we restrict further analysis to only those compounds that possess a favorable structure formation energy ($E^f[ABO_3] < 0$) and endothermic defect formation energies (in range [0,11eV]). This results in a list of fifteen compounds shown in Table.1. These fifteen

compounds obtained from the initial eighty compounds are likely to exhibit good proton transport properties.

For these restricted favorable compounds, we additionally calculate the dopant-vacancy interaction energies ($\Delta E^i[Y_B^0 - V_O^0 - Y_B^0]$), since the oxygen vacancies can get trapped near acceptor dopants[22,38] that can influence the hydration capacity of these doped perovskites. The PBE bandgap of these compounds are

provided in Table.S2 in SI where all of them possess a finite bandgap. The gap slightly increases with increasing A-site

ionic radius. Since, DFT using the PBE functional is notoriously known to under predict band-gaps,[61,62] this suggests that these compounds have good potential to be employed as electrolytes in PCFCs.

Defect Energies and Material Identities

To gain additional insights, we calculate the Pearson correlation coefficient between structural and defect energies, local distortions and material identities for this subset of compounds as shown in Fig.5. Fig.5(a) shows the correlation between the energies and material identities which is now expanded to include (i) tolerance factor with dopant ionic radius at B site (t_{DA}), (ii) ionic radius difference between dopant and B-site ($r_D - r_B$), (iii) χ difference between dopant and B-site ($\chi_D - \chi_B$), (iv) χ difference between dopant and A-site ($\chi_D - \chi_A$). Similar to the previous observation in the full dataset (Fig.1(c-d), $E^f[ABO_3]$ inversely correlates, and becomes more favorable with increasing values of t and $r_A + r_B$.

Interestingly, in case of these favorable compounds we observe new correlations between defect energies and material identities. $E^f[H_i^0]$ inversely correlates, and become more favorable with increasing tolerance factor

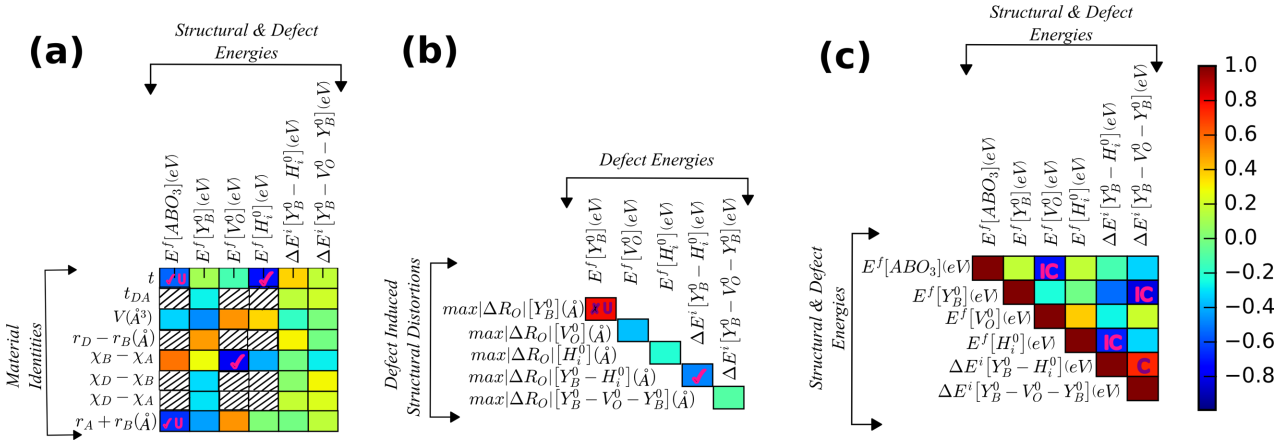

Figure.5 Correlation analysis among the fifteen potential perovskites to identify trends, where 1.0 indicates perfect positive correlation, -1.0 indicates perfect negative correlation and 0.0 indicates no correlation. (a) structure and defect energetics against material identities such as (i) tolerance factor (t) (ii) tolerance factor with dopant ionic radius at B site (t_{DA}), (iii)ionic radius difference between dopant and B-site ($r_D - r_B$) (iv) cationic electronegativity difference ($\chi_B - \chi_A$), (v) Electronegativity difference between dopant and B-site ($\chi_D - \chi_B$), (vi) Electronegativity difference between dopant and A-site ($\chi_D - \chi_A$), (vii) sum of cationic radius ($r_A + r_B$). The check mark indicates that the structure and defect energetics become more favorable as the material identities (such as t) increases. The symbol U indicates the correlation is universal, and is valid for the full dataset, comprising of both favorable and unfavorable perovskites. (b) Defect energetics against the induced local distortions as quantified by maximum displacement of O atom. The cross mark indicates that the $E^f[Y_B^0]$ becomes more unfavorable with distortion, while check mark indicates the dopant-H interaction becomes more attractive with increasing distortion. (c) Cross-correlation amongst the structure and defect energetics. The symbol C / IC respectively denotes correlation/inverse-correlation between the two variables.

Subset of cubic perovskites	$SrOsO_3$, $CaTiO_3$, $SrSnO_3$, $SrRuO_3$, $SrGeO_3$, $CaVO_3$, $SrMnO_3$, $SrHfO_3$, $SrZrO_3$, $SrTiO_3$, $SrVO_3$, $BaTiO_3$, $BaVO_3$, $BaHfO_3$, $BaZrO_3$,

Table. 1. Subset of fifteen cubic perovskites compounds with favorable structure formation ($E^f[ABO_3] < 0$) and endothermic defect formation ($E^f[Y_B^0]$, $E^f[V_O^0]$, $E^f[H_i^0]$ in range [0,11eV]).

(t), (i.e. R^2 = 0.52) as shown in Fig.6(b). This indicates that it is energetically favorable to introduce H interstitial in perovskites with large A site cations.

Similarly, Fig.6(a) shows that $E^f[V_O^0]$ decreases (O vacancy formation becomes more favorable) with increasing cationic electronegativity difference ($\chi_B - \chi_A$) (R^2=0.62). As the electronegativity of the B-site atom increases, its tendency to donate electron decreases, which likely leads to weaker bonding with oxygen atoms and smalle$E^f[V_O^0]$r. On the other hand, even for the subset of fifteen favorable compounds, dopant related energies ($E^f[Y_B^0]$, $\Delta E^i[Y_B^0 - H_i^0]$, $\Delta E^i[Y_B^0 - V_O^0 - Y_B^0]$) do not show any good quantitative correlation with the material identities indicating the challenges in creating simple and cheap descriptors to describe dopant related energies.

Defect Energies and Local Structural Distortions

Fig. 5(b) shows the correlation between defect energies and the induced local distortions. Like trends observed in the full dataset (Fig.3a), $E^f[Y_B^0]$ increases and positively correlates (dopant substitution becomes more unfavorable) with increasing local distortions

($max|\Delta R_O|[Y_B^0]$). However, for this subset, we also observe new correlations.

Fig. 6c shows that $\Delta E^i[Y_B^0 - H_i^0]$inverse correlates and becomes more negative (stronger dopant-H attraction) with increasing local distortion ($max|\Delta R_O|[Y_B^0 - H_i^0]$) with an R^2 value of 0.23. Although the R2 value is weak due to

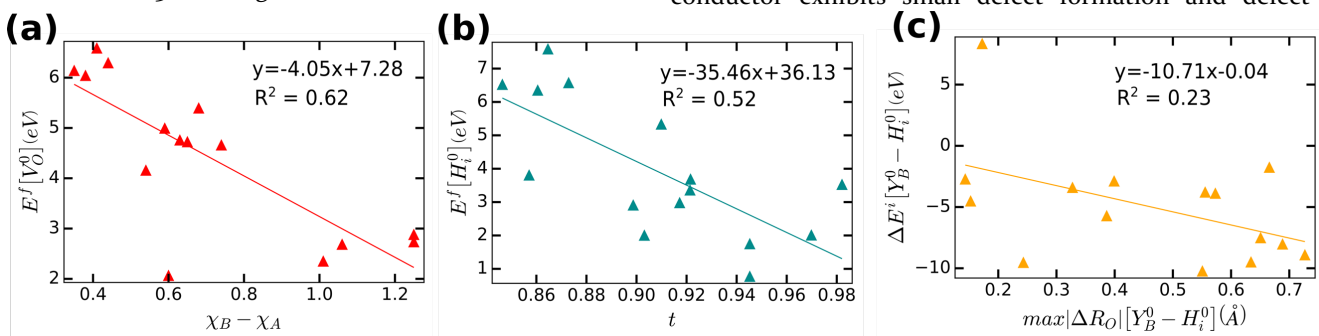

Figure.6. Scatter plot of energetics of the fifteen potential perovskites compounds along with linear regression fit. (a) Oxygen vacancy formation energy $(E^f[V_O^0])$ *decreases (becomes more favorable to form) with increasing cationic electronegativity difference* $(\chi_B - \chi_A)$ *(b) H interstitial formation energy* $(E^f[H_i^0])$ *decreases (becomes more favorable to form) with increasing tolerance factor (t). (c) Dopant-H interaction energy* $(\Delta E^i[Y_B^0 - H_i^0])$ *decreases (the interaction becomes more attractive), with increasing induced local structural distortion (quantified by the maximum oxygen displacement* $(max|\Delta R_O|[Y_B^0 - H_i^0])$.

few outliers, the insights from this correlation is consistent with previous literature. In Y doped $BaZrO_3$, previous works[21,63,64] have established the attractive interaction between proton interstitial and a wide range of acceptor dopants. These attractive interaction results in formation of hydrogen bonds ($O \cdots H$) through distortion of oxygen sub-lattice. The data described in Fig.6(d) shows that the phenomenon of hydrogen bond formation due to attractive dopant-H interaction is more generic across many perovskites compounds.

Cross Correlating Structural and Defect Energies

To design a new proton conductor, it is important to simultaneously optimize various structural and defect energies that influence proton transport. This in turn necessitates how these energies correlate with one another. Fig.5(c) shows the correlation between various energies with the detailed scatter plots shown in Fig.7. Fig.7(a) shows $E^f[V_O^0]$ inversely correlates (with R^2=0.50) with $E^f[ABO_3]$. Thus, the more stable a perovskite structure, the more difficult it is to create an oxygen vacancy. Fig.7(b) identifies that dopant-H interaction $\Delta E^i[Y_B^0 - H_i^0]$ inversely correlates with $E^f[H_i^0]$ (R^2 = 0.46). Similarly, Fig.7(c) identifies that dopant-vacancy interaction ($\Delta E^i[Y_B^0 - V_O^0 - Y_B^0]$) inversely correlates with $E^f[Y_B^0]$ (R2 = 0.67). This suggests that as forming isolated defects (H interstitial and Y dopant in this case) become more unfavorable, it becomes more favorable to form a dopant-defect complex. Further if a perovskite compound favors the formation of a dopant-H defect complex, it is also likely to favor the formation of dopant-vacancy complex as observed from the strong correlation between $\Delta E^i[Y_B^0 - H_i^0]$ and $\Delta E^i[Y_B^0 - V_O^0 - Y_B^0]$ as shown in Fig.7(d). However, such defect complex inherently possess strong attraction that leads to lowering of carrier (proton) concentration and mobility.

Perovskites with High Proton Conductivity

The energies of all these fifteen favorable compounds are plotted in Fig.8. As expected, $BaZrO_3$ a fast proton conductor exhibits small defect formation and defect interaction energies. On the other hand, $SrZrO_3$ that exhibits relatively lower proton conductivity,[28,65] exhibits stronger dopant-H attraction (-7.52eV for $SrZrO_3$ in comparison to -2.88eV for $BaZrO_3$), indicating proton trapping and reduced transport. From Fig.8, we observe that energies of three materials namely $BaTiO_3$, $BaVO_3$, $BaHfO_3$ are close to $BaZrO_3$, suggesting that these compounds are more likely to demonstrate fast proton transport in cubic perovskite phase.

Preliminary studies appear to validate this finding. Y doped $BaHfO_3$[66,67] appears to exhibit good proton transport properties. Similarly, cubic perovskite structures of $BaTiO_3$ stabilized through acceptor doping with Sc or In atoms[54,55] exhibit higher proton conductivity compared to other structural polymorphs. $BaVO_3$ under ambient conditions exhibits a hexagonal structure (*P-3m1*)[68]. However, it appears likely to stabilize cubic perovskite structure of the material at high pressures,[69] although no information is available regarding the stability of this phase upon proton uptake and its proton transport properties.

Density gradient based exchange correlation functional (PBE) are known to generate errors in bandgaps and defect transition levels of complex oxides. Thus, in order to ensure the robustness of the comparative analysis amongst various perovskite compounds and to qualitatively understand the uncertainty in defect energies in the current framework, we compare the PBE defect energies of four compounds namely $BaZrO_3$, $BaHfO_3$, BaTiO3 and $SrZrO_3$ against energies obtained from hybrid functional (HSE06), as shown in Table.2. We can observe from that PBE over-estimates favorability of dopant substitution ($E^f[Y_B^0]^{HSE} - E^f[Y_B^0]^{PBE} \in$ [2.14, 2.36] eV) and under-estimates favorability of vacancy formation ($E^f[V_O^0]^{HSE} - E^f[V_O^0]^{PBE} \in$ [-1.29, -2.10] eV). Similarly, PBE based

calculations also under-estimates the attractive interaction between dopant-H ($\Delta E^i[Y_B^0 - H_i^0]^{HSE} - \Delta E^i[Y_B^0 - H_i^0]^{PBE} \in$ [-0.09, -1.46] eV) and dopant-vacancies ($\Delta E^i[Y_B^0 - V_O^0 - Y_B^0]^{HSE} - \Delta E^i[Y_B^0 - V_O^0 - Y_B^0]^{HSE} \in$ [-1.15, -3.19] eV).

More importantly, this comparison enables us to validate that the current methodology based on PBE captures the trends across compounds for all the defect energies studied in this work. Accordingly, the methodology correctly identifies that it is more difficult to dope SrZrO3 than compared to BaZrO3 and that the formation of defect-complex is more likely in SrZrO3 compared to BaZrO3 that explains the poor proton conductivity in SrZrO3. Thus, the current computational framework is robust in identifying potential compounds that can exhibit good proton transport property.

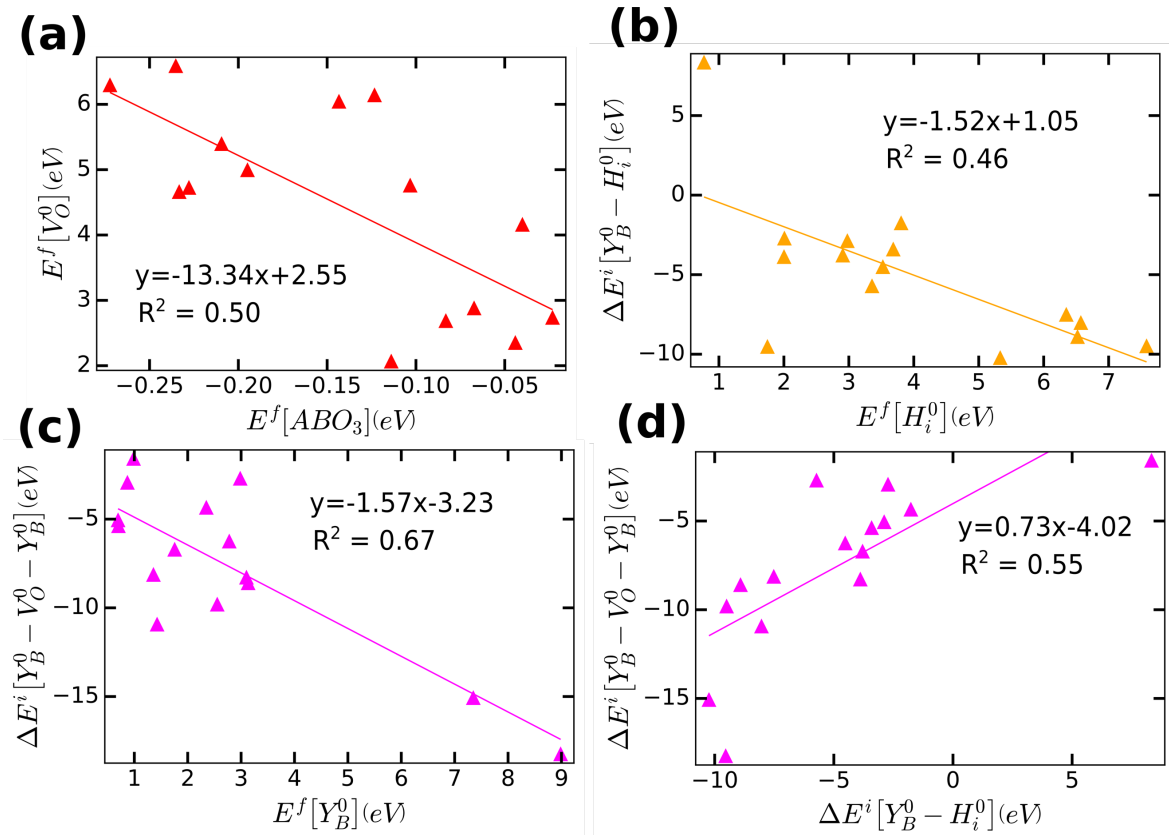

Figure.7 Scatter plot of energetics of the fifteen potential perovskites compounds along with linear regression fit. (a) Oxygen vacancy formation energy ($E^f[V_O^0]$) decreases (becomes more favorable to form) with increasing (unfavorable) structure formation energy ($E^f[ABO_3]$) (b) Dopant-H interaction energy ($\Delta E^i[Y_B^0 - H_i^0]$) decreases (the interaction becomes more attractive) with increasing (unfavorable) H interstitial formation energy ($E^f[H_i^0]$). (c) Dopant-vacancy interaction energy ($\Delta E^i[Y_B^0 - V_O^0 - Y_B^0]$) decreases (the interaction becomes more attractive) with increasing (unfavorable) Dopant substitution energy ($E^f[Y_B^0]$). (d) Dopant-vacancy interaction energy ($\Delta E^i[Y_B^0 - V_O^0 - Y_B^0]$) increases (the interaction becomes less attractive) with increasing (less attractive) Dopant-H interaction energy ($\Delta E^i[Y_B^0 - H_i^0]$).

SUMMARY & CONCLUSIONS

To summarize, we develop a computational framework, where highly scalable workflows are employed, to perform *ab initio* calculations, to systematically study (i) structure formation energy ($E^f[ABO_3]$), (ii) defect formation energies (yttrium dopant substitution ($E^f[Y_B^0]$), oxygen vacancy formation ($E^f[V_O^0]$), H interstitial formation ($E^f[H_i^0]$)), and (iii) defect interaction energy (dopant-H $\Delta E^i[Y_B^0 - H_i^0]$) in over eighty (2,4) cubic perovskites.

$E^f[ABO_3]$ and endothermic defect formation energies (in range [0,11] eV) exhibit inverse correlations (becomes more favorable to form) with increasing values of material identities, such as (a) $E^f[ABO_3]$ (vs) t, (b) $E^f[ABO_3]$ (vs) $r_A + r_B$ and (c) $E^f[H_i^0]$ (vs) t. The intersection of favorable $E^f[ABO_3]$ (< 0eV) and endothermic defect formation energies (in range [0,11eV]) identifies a subset of fifteen promising favorable compounds. For these favorable compounds, we also calculate the dopant-vacancy interaction energy ($\Delta E^i[Y_B^0 - V_O^0 - Y_B^0]$). Data from this subset identifies new correlations with material identities, (such as $E^f[V_O^0]$ (vs) $\chi_B - \chi_A$ and $E^f[H_i^0]$ vs t), that were previously suppressed in the full dataset by presence of unfavorable compounds.

The defect energies of this subset when correlated with the defect induced local distortions help elucidate the mechanisms that influence defect formation and interaction, such as (a) local strain in $E^f[Y_B^0]$, and (b) hydrogen bonding in $\Delta E^i[Y_B^0 - H_i^0]$). We also identify various inverse correlations between energies, such as, (a) $E^f[V_O^0]$ (vs) $E^f[ABO_3]$, (b) $\Delta E^i[Y_B^0 - H_i^0]$ (vs) $E^f[H_i^0]$ and

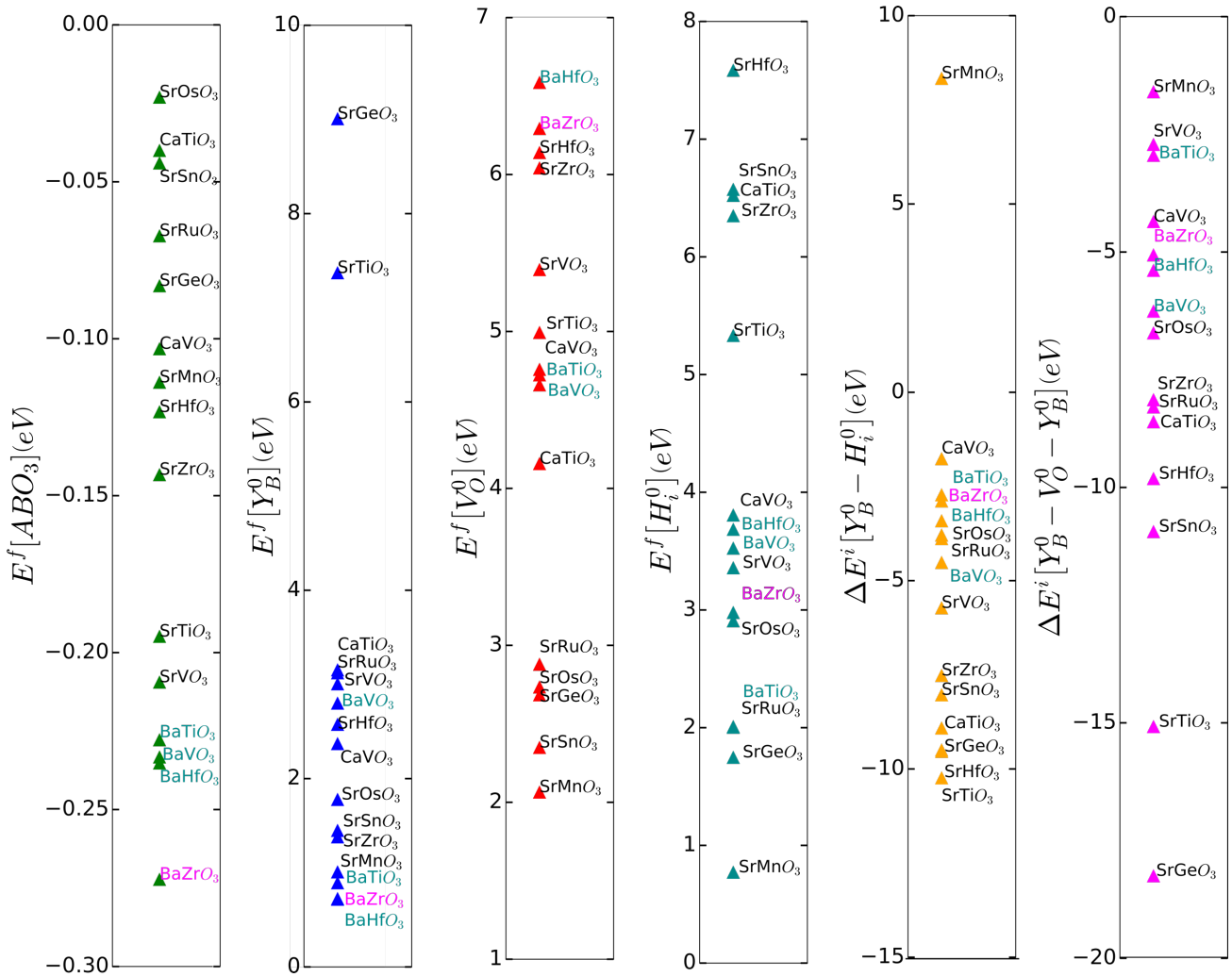

Figure.8 Structure and defect energetics for the fifteen potential perovskite compounds compared against the most commonly studied proton conductor $BaZrO_3$. Three systems namely $BaTiO_3$, $BaVO_3$ and $BaHfO_3$ are identified to have similar energetics as BaZrO3 and hence are expected to exhibit high proton conductivity.

Perovskites Compounds	PBE Defect Energies (eV)					HSE Defect Energies (eV)				
	$E^f[Y_B^0]$	$E^f[V_O^0]$	$E^f[H_i^0]$	$\Delta E^i[Y_B^0 - H_i^0]$	$\Delta E^i[Y_B^0 - V_O^0 - Y_B^0]$	$E^f[Y_B^0]$	$E^f[V_O^0]$	$E^f[H_i^0]$	$\Delta E^i[Y_B^0 - H_i^0]$	$\Delta E^i[Y_B^0 - V_O^0 - Y_B^0]$
$BaTiO_3$	0.89	4.72	2.01	-2.95	-2.73	3.17	2.62	1.06	-4.09	-2.82
$BaZrO_3$	0.72	6.29	2.98	-5.06	-2.89	3.04	5.19	3.57	-8.26	-4.11
$BaHfO_3$	0.72	6.59	3.68	-5.39	-3.41	3.09	5.30	4.08	-8.24	-4.88
$SrZrO_3$	1.38	6.04	6.35	-8.14	-7.52	3.52	4.63	6.94	-10.52	-8.91

Table.2. Comparison of defect energies between PBE based current methodology and hybrid (HSE) based calculations for four different compounds identifies that the trends in defect energies are similar for the two exchange-correlation functionals.

(c) $\Delta E^i[Y_B^0 - V_O^0 - Y_B^0]$ (vs) $E^f[Y_B^0]$. We also identify the positive correlation between $\Delta E^i[Y_B^0 - H_i^0]$ and $\Delta E^i[Y_B^0 - V_O^0 - Y_B^0]$. These correlations highlight the tradeoffs and illuminate us on the challenges in simultaneously optimizing competing structural and defect energies for high proton conductivity. Finally, comparing the energies of the compounds against BaZrO3 enables us to narrow down to three perovskite compounds namely BaTiO3, BaVO3, BaHfO3 that are expected to exhibit fast proton transport.

To conclude, the genomic point defect data and the insightful correlations generated by this high-throughput computational framework, can be envisioned to be fed into computationally inexpensive machine-learning models,

that can accelerate predictions of defect energetics. This combination could then be used to expand the search for new proton conductors not only across different dopants, but also across other crystal structures such as double-perovskites, pyrochlores, fluorites etc. Similar approaches can also be employed to systematically screen functional defects and its influence on material properties for other energy applications such as hydrogen storage, CO_2 capture, solid state lighting, thermoelectrics and solid-state batteries.

ASSOCIATED CONTENT

Supporting Information

The Supporting Information is available free of charge on the ACS Publications website.

Computational details; Additional results comprising of heatmap and scatter plots correlating structural and defect energies, material identities and defect induced local distortions.

AUTHOR INFORMATION

Corresponding Author

*balachandraj@ornl.gov
*ganeshp@ornl.gov

ACKNOWLEDGMENT

This research was sponsored by the Laboratory Directed Research and Development Program (LDRD) of Oak Ridge National Laboratory, managed by UT-Battelle, LLC, for the U. S. Department of Energy. This research used resources of the Oak Ridge Leadership Computing Facility at the Oak Ridge National Laboratory, which is supported by the Office of Science of the U.S. Department of Energy under Contract No. DE-AC05-00OR22725. The authors would like to thank the developers of wraprun – Matt Belhorn and Adam Simpson for their help and support in enabling the integration of wraprun with the workflow.

REFERENCES

(1) Curtarolo, S.; Hart, G. L. W.; Nardelli, M. B.; Mingo, N.; Sanvito, S.; Levy, O. The High-Throughput Highway to Computational Materials Design. *Nat. Mater.* **2013**, *12* (3), 191–201.

(2) Ceder, G. Opportunities and Challenges for First-Principles Materials Design and Applications to Li Battery Materials. *MRS Bull.* **2010**, *35* (09), 693–701.

(3) Jain, A.; Ong, S. P.; Hautier, G.; Chen, W.; Richards, W. D.; Dacek, S.; Cholia, S.; Gunter, D.; Skinner, D.; Ceder, G.; et al. Commentary: The Materials Project: A Materials Genome Approach to Accelerating Materials Innovation. *APL Mater.* **2013**, *1* (1), 011002.

(4) Calderon, C. E.; Plata, J. J.; Toher, C.; Oses, C.; Levy, O.; Fornari, M.; Natan, A.; Mehl, M. J.; Hart, G.; Buongiorno Nardelli, M.; et al. The AFLOW Standard for High-Throughput Materials Science Calculations. *Comput. Mater. Sci.* **2015**, *108*, 233–238.

(5) Olson, G. B. Genomic Materials Design: The Ferrous Frontier. *Acta Mater.* **2013**, *61* (3), 771–781.

(6) Saal, J. E.; Kirklin, S.; Aykol, M.; Meredig, B.; Wolverton, C. Materials Design and Discovery with High-Throughput Density Functional Theory: The Open Quantum Materials Database (OQMD). *JOM* **2013**, *65* (11), 1501–1509.

(7) Ghiringhelli, L. M.; Carbogno, C.; Levchenko, S.; Mohamed, F.; Huhs, G.; Lüders, M.; Oliveira, M.; Scheffler, M. Towards a Common Format for Computational Material Science Data. *ArXiv Prepr. ArXiv160704738* **2016**.

(8) Dunstan, M. T.; Jain, A.; Liu, W.; Ong, S. P.; Liu, T.; Lee, J.; Persson, K. A.; Scott, S. A.; Dennis, J. S.; Grey, C. P. Large Scale Computational Screening and Experimental Discovery of Novel Materials for High Temperature CO_2 Capture. *Energy Env. Sci* **2016**, *9* (4), 1346–1360.

(9) de Jong, M.; Chen, W.; Geerlings, H.; Asta, M.; Persson, K. A. A Database to Enable Discovery and Design of Piezoelectric Materials. *Sci. Data* **2015**, *2*, 150053.

(10) Perim, E.; Lee, D.; Liu, Y.; Toher, C.; Gong, P.; Li, Y.; Simmons, W. N.; Levy, O.; Vlassak, J. J.; Schroers, J.; et al. Spectral Descriptors for Bulk Metallic Glasses Based on the Thermodynamics of Competing Crystalline Phases. *ArXiv Prepr. ArXiv160601162* **2016**.

(11) Yu, L.; Zunger, A. Identification of Potential Photovoltaic Absorbers Based on First-Principles Spectroscopic Screening of Materials. *Phys. Rev. Lett.* **2012**, *108* (6).

(12) Crawford, J. H.; Slifkin, L. M. *Point Defects in Solids: General and Ionic Crystals*; Springer Science & Business Media, 2013.

(13) Tuller, H. L.; Bishop, S. R. Point Defects in Oxides: Tailoring Materials Through Defect Engineering. *Annu. Rev. Mater. Res.* **2011**, *41* (1), 369–398.

(14) Freysoldt, C.; Grabowski, B.; Hickel, T.; Neugebauer, J.; Kresse, G.; Janotti, A.; Van de Walle, C. G. First-Principles Calculations for Point Defects in Solids. *Rev. Mod. Phys.* **2014**, *86* (1), 253–305.

(15) Sharma, V.; Wang, C.; Lorenzini, R. G.; Ma, R.; Zhu, Q.; Sinkovits, D. W.; Pilania, G.; Oganov, A. R.; Kumar, S.; Sotzing, G. A.; et al. Rational Design of All Organic Polymer Dielectrics. *Nat. Commun.* **2014**, *5*, 4845.

(16) de Jong, M.; Chen, W.; Notestine, R.; Persson, K.; Ceder, G.; Jain, A.; Asta, M.; Gamst, A. A Statistical Learning Framework for Materials Science: Application to Elastic Moduli of k-Nary Inorganic Polycrystalline Compounds. *Sci. Rep.* **2016**, *6*, 34256.

(17) Rupp, M.; Tkatchenko, A.; Müller, K.-R.; von Lilienfeld, O. A. Fast and Accurate Modeling of Molecular Atomization Energies with Machine Learning. *Phys. Rev. Lett.* **2012**, *108* (5).

(18) Ertekin, E.; Srinivasan, V.; Ravichandran, J.; Rossen, P. B.; Siemons, W.; Majumdar, A.; Ramesh, R.; Grossman, J. C. Interplay between Intrinsic Defects, Doping, and Free Carrier Concentration in SrTiO 3 Thin Films. *Phys. Rev. B* **2012**, *85* (19).

(19) Kumagai, Y.; Oba, F. Electrostatics-Based Finite-Size Corrections for First-Principles Point Defect Calculations. *Phys. Rev. B* **2014**, *89* (19).

(20) Emery, A. A.; Saal, J. E.; Kirklin, S.; Hegde, V. I.; Wolverton, C. High-Throughput Computational Screening of Perovskites for Thermochemical Water Splitting Applications. *Chem. Mater.* **2016**, *28* (16), 5621–5634.

(21) Björketun, M. E.; Sundell, P. G.; Wahnström, G. Effect of Acceptor Dopants on the Proton Mobility in Ba Zr O 3 : A Density Functional Investigation. *Phys. Rev. B* **2007**, *76* (5).

(22) Ding, J.; Balachandran, J.; Sang, X.; Wei Guo, J. S. A.; Veith, G. M.; Bridges, C. A.; Cheng, Y.; Rouleau, C. M.; Poplawsky, J. D.; Bassiri-Gharb1, N.; et al. Origin of Fast Proton Transport in Stoichiometric Acceptor Doped Perovskites. *Rev.*

(23) Jain, A.; Ong, S. P.; Chen, W.; Medasani, B.; Qu, X.; Kocher, M.; Brafman, M.; Petretto, G.; Rignanese, G.-M.; Hautier, G.; et al. FireWorks: A Dynamic Workflow System Designed for High-Throughput Applications: FireWorks: A Dynamic Workflow System Designed for High-Throughput Applications. *Concurr. Comput. Pract. Exp.* **2015**, *27* (17), 5037–5059.

(24) Ormerod, R. M. Solid Oxide Fuel Cells. *Chem. Soc. Rev.* **2003**, *32* (1), 17–28.

(25) Wachsman, E. D.; Lee, K. T. Lowering the Temperature of Solid Oxide Fuel Cells. *Science* **2011**, *334* (6058), 935–939.

(26) Goodenough, J. B. Oxide-Ion Electrolytes. *Annu. Rev. Mater. Res.* **2003**, *33* (1), 91–128.

(27) Huang, K.; Goodenough, J. B. *Solid Oxide Fuel Cell Technology: Principles, Performance and Operations*; Elsevier, 2009.

(28) Kreuer, K. D. Proton-Conducting Oxides. *Annu. Rev. Mater. Res.* **2003**, *33*, 333–359.

(29) Fabbri, E.; Bi, L.; Pergolesi, D.; Traversa, E. Towards the Next Generation of Solid Oxide Fuel Cells Operating Below 600 °C with Chemically Stable Proton-Conducting Electrolytes. *Adv. Mater.* **2012**, *24* (2), 195–208.

(30) Malavasi, L.; Fisher, C. A. J.; Islam, M. S. Oxide-Ion and Proton Conducting Electrolyte Materials for Clean Energy Applications: Structural and Mechanistic Features. *Chem. Soc. Rev.* **2010**, *39* (11), 4370.

(31) Yamazaki, Y.; Blanc, F.; Okuyama, Y.; Buannic, L.; Lucio-Vega, J. C.; Grey, C. P.; Haile, S. M. Proton Trapping in Yttrium-Doped Barium Zirconate. *Nat. Mater.* **2013**, *12* (7), 647–651.

(32) Iwahara, H.; Uchida, H.; Maeda, N. High Temperature Fuel and Steam Electrolysis Cells Using Proton Conductive Solid Electrolytes. *J. Power Sources* **1982**, *7* (3), 293–301.

(33) Norby, T.; Kofstad, P. Proton and Native-Ion Conductivities in Y2O3 at High Temperatures. *Solid State Ion.* **1986**, *20* (3), 169–184.

(34) Kreuer, K.-D.; Münch, W.; Fuchs, A.; Klock, U.; Maier, J.; others. Proton Conducting Alkaline Earth Zirconates and Titanates for High Drain Electrochemical Applications. *Solid State Ion.* **2001**, *145* (1), 295–306.

(35) Duan, C.; Tong, J.; Shang, M.; Nikodemski, S.; Sanders, M.; Ricote, S.; Almansoori, A.; O'Hayre, R. Readily Processed Protonic Ceramic Fuel Cells with High Performance at Low Temperatures. *Science* **2015**, *349* (6254), 1321–1326.

(36) Lindman, A.; Erhart, P.; Wahnström, G. Implications of the Band Gap Problem on Oxidation and Hydration in Acceptor-Doped Barium Zirconate. *Phys. Rev. B* **2015**, *91* (24).

(37) Chase, M. W. JANAF Thermochemical Tables. *JANAF Thermochem. Tables Chase MW Wash. DC Am. Chem. Soc. N. Y. Am. Inst. Phys. Natl. Bur. Stand. C1986 U. S. Natl. Bur. Stand.* **1986**.

(38) Björketun, M. E.; Sundell, P. G.; Wahnström, G. Structure and Thermodynamic Stability of Hydrogen Interstitials in $BaZrO_3$ Perovskite Oxide from Density Functional Calculations. *Faraday Discuss* **2007**, *134*, 247–265.

(39) Jilai Ding; Janakiraman Balachandran; Xiahan Sang; Wei Guo; Jonathan A. Anchell; Gabriel M. Veith; Craig A. Bridges; Yongqiang Cheng; Christopher M. Rouleau; Jonathan D. Poplawsky; et al. Origin of Fast Proton Transport in Stoichiometric Acceptor Doped Perovskites.

(40) Freysoldt, C.; Neugebauer, J.; Van de Walle, C. G. Fully *Ab Initio* Finite-Size Corrections for Charged-Defect Supercell Calculations. *Phys. Rev. Lett.* **2009**, *102* (1).

(41) Goyal, A.; Gorai, P.; Peng, H.; Lany, S.; Stevanović, V. A Computational Framework for Automation of Point Defect Calculations. *Comput. Mater. Sci.* **2017**, *130*, 1–9.

(42) Lany, S.; Zunger, A. Assessment of Correction Methods for the Band-Gap Problem and for Finite-Size Effects in Supercell Defect Calculations: Case Studies for ZnO and GaAs. *Phys. Rev. B* **2008**, *78* (23).

(43) Leslie, M.; Gillan, N. The Energy and Elastic Dipole Tensor of Defects in Ionic Crystals Calculated by the Supercell Method. *J. Phys. C Solid State Phys.* **1985**, *18* (5), 973.

(44) Kresse, G.; Furthmüller, J. Efficient Iterative Schemes for Ab Initio Total-Energy Calculations Using a Plane-Wave Basis Set. *Phys. Rev. B* **1996**, *54* (16), 11169.

(45) Kresse, G.; Furthmüller, J. Efficiency of Ab-Initio Total Energy Calculations for Metals and Semiconductors Using a Plane-Wave Basis Set. *Comput. Mater. Sci.* **1996**, *6*, 15–50.

(46) Perdew, J. P.; Burke, K.; Ernzerhof, M. Generalized Gradient Approximation Made Simple. *Phys. Rev. Lett.* **1996**, *77* (18), 3865.

(47) Blöchl, P. E. Projector Augmented-Wave Method. *Phys. Rev. B* **1994**, *50* (24), 17953.

(48) Sundell, P. G.; Björketun, M. E.; Wahnström, G. Thermodynamics of Doping and Vacancy Formation in BaZrO 3 Perovskite Oxide from Density Functional Calculations. *Phys. Rev. B* **2006**, *73* (10).

(49) Ong, S. P.; Richards, W. D.; Jain, A.; Hautier, G.; Kocher, M.; Cholia, S.; Gunter, D.; Chevrier, V. L.; Persson, K. A.; Ceder, G. Python Materials Genomics (Pymatgen): A Robust, Open-Source Python Library for Materials Analysis. *Comput. Mater. Sci.* **2013**, *68*, 314–319.

(50) olcf/wraprun https://github.com/olcf/wraprun (accessed Dec 14, 2016).

(51) Heyd, J.; Scuseria, G. E.; Ernzerhof, M. Hybrid Functionals Based on a Screened Coulomb Potential. *J. Chem. Phys.* **2003**, *118* (18), 8207–8215.

(52) Paier, J.; Marsman, M.; Hummer, K.; Kresse, G.; Gerber, I. C.; Ángyán, J. G. Screened Hybrid Density Functionals Applied to Solids. *J. Chem. Phys.* **2006**, *124* (15), 154709.

(53) Sasaki, S.; Prewitt, C. T.; Bass, J. D.; Schulze, W. Orthorhombic Perovskite CaTiO3 and CdTiO3: Structure and Space Group. *Acta Crystallogr. C* **1987**, *43* (9), 1668–1674.

(54) Bjørheim, T. S.; Rahman, S. M. H.; Eriksson, S. G.; Knee, C. S.; Haugsrud, R. Hydration Thermodynamics of the Proton Conducting Oxygen-Deficient Perovskite Series $BaTi_{1-x}M_xO_{3-x/2}$ with M = In or Sc. *Inorg. Chem.* **2015**, *54* (6), 2858–2865.

(55) Rahman, S. M. H.; Norberg, S. T.; Knee, C. S.; Biendicho, J. J.; Hull, S.; Eriksson, S. G. Proton Conductivity of Hexagonal and Cubic $BaTi_{1-x}Sc_xO_{3-\delta}$ ($0.1 \leq x \leq 0.8$). *Dalton Trans* **2014**, *43* (40), 15055–15064.

(56) Cheng, J.-G.; Alonso, J. A.; Suard, E.; Zhou, J.-S.; Goodenough, J. B. A New Perovskite Polytype in the High-Pressure Sequence of $BaIrO_3$. *J. Am. Chem. Soc.* **2009**, *131* (21), 7461–7469.

(57) Yildiz, B. "Stretching" the Energy Landscape of Oxides—Effects on Electrocatalysis and Diffusion. *MRS Bull.* **2014**, *39* (02), 147–156.

(58) Glazer, A. M. The Classification of Tilted Octahedra in Perovskites. *Acta Crystallogr. B* **1972**, *28* (11), 3384–3392.

(59) Glazer, A. M. Simple Ways of Determining Perovskite Structures. *Acta Crystallogr. A* **1975**, *31* (6), 756–762.

(60) Li, C.; Soh, K. C. K.; Wu, P. Formability of ABO3 Perovskites. *J. Alloys Compd.* **2004**, *372* (1–2), 40–48.

(61) Chan, M. K. Y.; Ceder, G. Efficient Band Gap Prediction for Solids. *Phys. Rev. Lett.* **2010**, *105* (19).

(62) Gopal, P.; Fornari, M.; Curtarolo, S.; Agapito, L. A.; Liyanage, L. S. I.; Nardelli, M. B. Improved Predictions of the Physical Properties of Zn- and Cd-Based Wide Band-Gap Semiconductors: A Validation of the ACBN0 Functional. *Phys. Rev. B* **2015**, *91* (24).

(63) Kang, S. G.; Sholl, D. S. First Principles Assessment of Perovskite Dopants for Proton Conductors with Chemical Stability and High Conductivity. *RSC Adv.* **2013**, *3* (10), 3333.

(64) Stokes, S. J.; Islam, M. S. Defect Chemistry and Proton-Dopant Association in BaZrO3 and BaPrO3. *J. Mater. Chem.* **2010**, *20* (30), 6258.

(65) Norby, T.; Larring, Y. Concentration and Transport of Protons in Oxides. *Curr. Opin. Solid State Mater. Sci.* **1997**, *2* (5), 593–599.

(66) Kang, S. G.; Sholl, D. S. Characterizing Chemical Stability and Proton Conductivity of B-Site Doped Barium Hafnate (BaHfO3) and Barium Stannate (BaSnO3) with First Principles Modeling. *J. Alloys Compd.* **2017**, *693*, 738–743.

(67) Snijkers, F. M. M.; Buekenhoudt, A.; Luyten, J. J.; Cooymans, J.; Mertens, M. Proton Conductivity in Perovskite Type Yttrium Doped Barium Hafnate. *Scr. Mater.* **2004**, *51* (12), 1129–1134.

(68) Liu, G.; Greedan, J. E. Syntheses, Structures, and Characterization of 5-Layer BaVO 3-x (X= 0.2, 0.1, 0.0). *J. Solid State Chem.* **1994**, *110* (2), 274–289.

(69) Nishimura, K.; Yamada, I.; Oka, K.; Shimakawa, Y.; Azuma, M. High-Pressure Synthesis of BaVO3: A New Cubic Perovskite. *J. Phys. Chem. Solids* **2014**, *75* (6), 710–712.
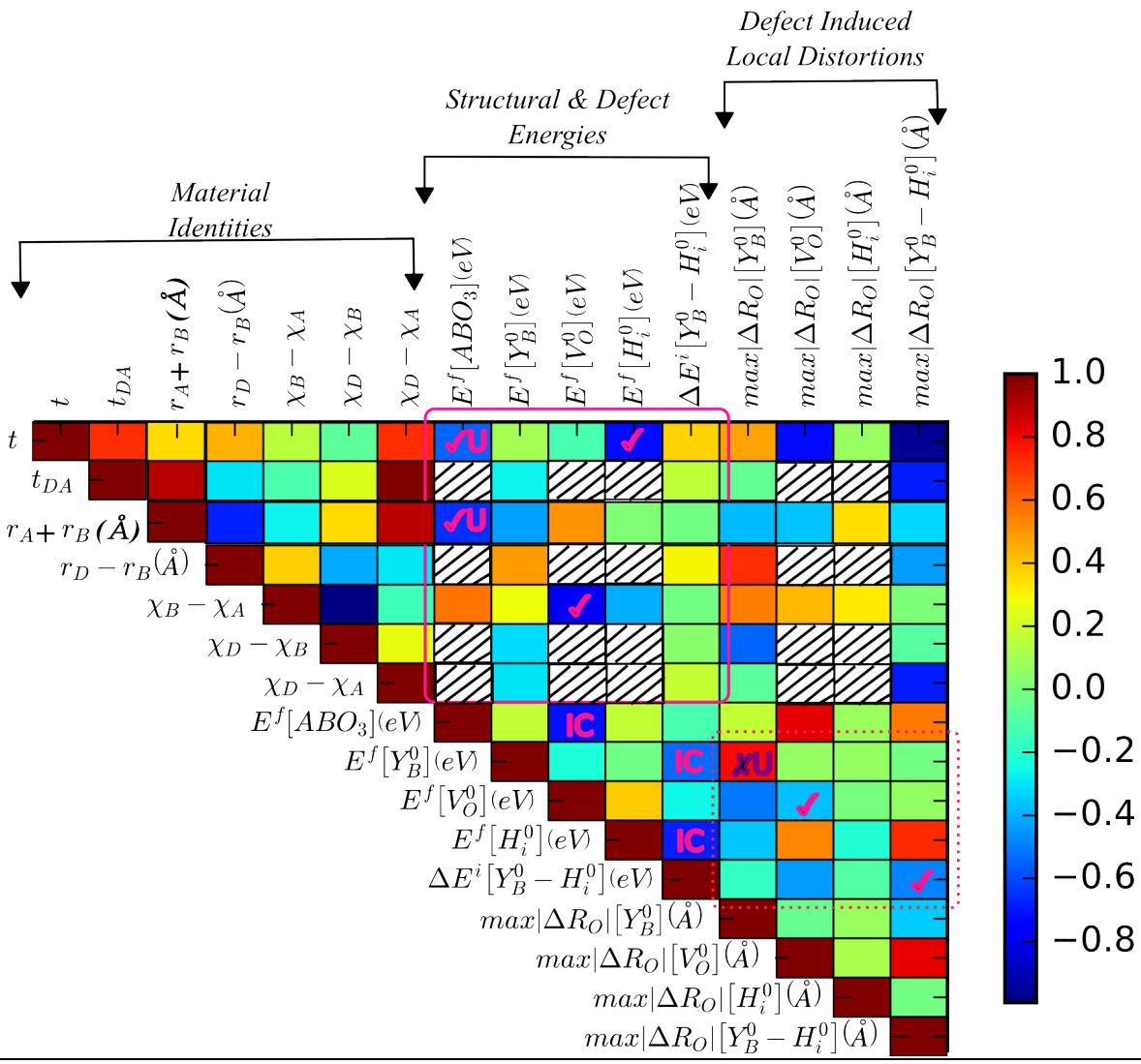
Insert Table of Contents artwork here